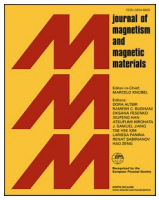
Journal of Magnetism and Magnetic Materials 630 (2025) 173439



Contents lists available at ScienceDirect

Journal of Magnetism and Magnetic Materials

journal homepage: www.elsevier.com/locate/jmmm



Research article

# An improved J-A model for iron-based soft magnetic composites considering local demagnetization effect

Zhang Changgeng [a], Guo Ziran [a], Lin Zhiwei [a,b,*], Li Yongjian [a]

[a] State Key Laboratory of Intelligent Power Distribution Equipment and System, Hebei University of Technology, Tianjin 300401, PR China
[b] Ningbo Magnetic Materials Application Technology Innovation Center Co., Ltd, Ningbo 315100 Zhejiang, PR China

ARTICLE INFO

*Keywords:*
Soft magnetic composites
J-A hysteresis model
Magnetization mechanism

ABSTRACT

Soft magnetic composites (SMCs), as three-dimensional (3D) isotropic materials can serve as substitutes for traditional laminated soft magnetic materials especially in 3D magnetic circuit devices such as claw-pole motors and power electronics. To utilize and optimize the properties of iron-based SMCs, it is essential to accurately model their magnetic properties at low frequencies and near saturation magnetic flux density. This paper proposes an improved J-A (Jiles-Atherton) model that predicts magnetization in SMCs by considering the influence of internal demagnetization on domain wall motion, incorporating an effective demagnetization factor to adjust the effective field. Simultaneously, a dynamic hysteresis model applicable to SMCs is established for the inter-particle and intra-particle eddy current losses of SMCs. Two iron-based SMC samples with 5 wt% and 7.5 wt% Ni-Zn ferrite content were fabricated via spark plasma sintering (SPS) and tested under static and dynamic magnetization of in-service conditions. A comparative analysis of experiments and simulations shows that the improved model accurately predicts hysteresis loops and iron losses, with relative errors under 8 % in the 10–100 Hz frequency range, which improvements are especially noticeable at the near saturable area of the simulation loop.

## 1. Introduction

Soft magnetic composites (SMCs) are advanced materials with unique structural and functional properties that have gained significant attention in recent years [1–6]. These composites consist of a ferromagnetic powder matrix coated with high-resistivity insulating layers. The materials are processed through powder metallurgy techniques to form complex three-dimensional geometries. A defining feature of SMCs lies in the electrical isolation of individual ferromagnetic particles by insulating layers, which disrupts interparticle conductive pathways. This architecture significantly suppresses eddy current generation, thereby markedly reducing iron losses under high-frequency excitation and extending the operational frequency range of soft magnetic materials [7]. SMCs exhibit three-dimensional isotropic magnetic properties, unlike conventional laminated materials. This makes them suitable for applications in high-frequency transformers, motors, inductors, power electronic converters, and other devices [8]. Among them, iron-based SMCs are mainly used in high-power electromagnetic devices with low frequency (≤100 Hz) and high magnetic flux density [8]. Advances in powder metallurgy have reduced the time and cost of producing SMCs, suggesting a promising future for their industrial adoption and technological use.

However, the magnetization of SMCs differs significantly from that of conventional soft magnetic materials. Due to the presence of insulating coating layers and a certain number of air pores inside the SMCs. The ferromagnetic powder matrix, which is the primary magnetization contributor, exists as discrete, magnetically isolated particles. As a result, magnetization occurs within individual ferromagnetic particle, operating independently from neighboring particles with minimal magnetic coupling [9]. During magnetization, the interfacial magnetic polarization at the insulating boundaries induces localized demagnetization fields, while the geometric anisotropy of individual particles further amplifies particle-specific demagnetization effects. These combined phenomena require substantially stronger external magnetic fields to achieve saturation, with the required field intensities exceeding those of conventional soft magnetic materials by one to three orders of magnitude [10]. Therefore, it is essential to consider the specificity of these materials when conducting analytical calculations and

* Corresponding author at: State Key Laboratory of Intelligent Power Distribution Equipment and System, Hebei University of Technology, Tianjin 300401, PR China.
*E-mail address:* jacklin7310@hotmail.com (L. Zhiwei).

https://doi.org/10.1016/j.jmmm.2025.173439
Received 7 April 2025; Received in revised form 3 August 2025; Accepted 14 August 2025
Available online 14 August 2025
0304-8853/© 2025 Elsevier B.V. All rights are reserved, including those for text and data mining, AI training, and similar technologies.

establishing hysteresis models for SMCs.

Since SMCs are primarily composed of ferromagnetic materials, which exhibit complex nonlinear hysteresis. Accurately constructing hysteresis models is essential for their use in electromagnetic components and device optimization. Currently, the hysteresis models predominantly apply to ferromagnetic materials include the Preisach model, Jiles Etherton (J-A) model, neural network model and Energetic model [11]. The Preisach and neural network model, as mathematical models, offer high accuracy, demonstrates superior predictive accuracy in hysteresis characterization but encounters significant challenges in parameter identification [12]. The J-A model and Energetic model, as physical models, consider the physical magnetization process. Specifically, the Energetic model is primarily suitable for conditions requiring high-precision energy analysis [13]. Nevertheless, in practical applications, the J-A model is comparatively easy to implement and has a low computational cost [14], rendering it a more viable candidate for accurate modeling and magnetic property prediction of SMCs. The initially proposed J-A model is a static model that only considers hysteresis losses. In 1993, D. Jiles incorporated classical eddy current losses and excess losses into the energy balance equation based on the energy conservation relationship during magnetization, thereby deriving a frequency-dependent dynamic J-A model [15]. However, unlike classical ferromagnetic materials, Kollar divided eddy current losses in SMCs into inter-particle eddy current losses and intra-particle eddy current losses [7]. Thus, when developing a dynamic J-A model for SMCs, it is crucial to account for these unique dynamic loss characteristics.

For the application of the J-A model in SMCs, the influence of the demagnetization field on magnetization firstly be considered to simulate their anhysteretic magnetization characteristics [16]. The static J-A model was improved by introducing a surface demagnetization factor and applied to various iron-based SMCs containing organic insulation coatings, nanocrystals, amorphous components, etc. Another improved J-A model for SMCs introduced excitation factors related to magnetic flux density and used DEM numerical simulations, enabling quantitative determination of critical parameters such as consolidated material density [17]. Based on these parameters, the static and dynamic hysteresis loops of commercial SMCs can be accurately modelled. This improved J-A model demonstrates remarkable predictive capability for simulating both static and dynamic hysteresis loop characteristics in commercial-grade SMCs. Compared with these models, the traditional J-A model has strong engineering practicability and high recognition, so this paper selects the traditional J-A model for comparison.

Although numerous modeling methodologies have been established for commercial SMCs [18–20], substantial iron losses discrepancies persist in laboratory prepared SMCs. Recent research efforts have focused on developing SMCs with enhanced performance. A versatile hysteresis model can offer additional benefits by reducing workload and resource consumption. To address this need, this study first uses a spark plasma sintering (SPS) device to produce two distinct types of Ni-Zn ferrite content iron-based SMC samples, and uses a hysteresis loop measuring instrument to measure the hysteresis loops of the SMC samples under quasi-static and different frequency sine excitations. Second, based on the significant influence of the internal demagnetization field on the magnetization of SMCs, geometry-dependent demagnetization coefficients are introduced to correct the effective field. In addition, a dynamic J-A model suitable for SMCs is established based on the field separation approach, considering the special eddy current loss mechanism of SMCs. Considering that iron-based SMCs are mainly used at low frequencies and saturation magnetic flux densities, the accuracy of the improved model under in-service conditions has been verified through experimental data.

## 2. Experimental method

SMC powders were produced by ball milling a mixture of pure iron powder with 5 wt% and 7.5 wt% Ni-Zn ferrite powders, respectively, resulting in iron particles coated with ferrite. Using SPS device, the temperature is raised to 670 ℃ at a rate of 60℃/min under a pressure of 40 MPa, and maintained for 5 min. Subsequently, the samples are cooled to room temperature. The sintering process is conducted in a vacuum environment, and the relevant parameters of the two samples are listed in Table 1. After basic mechanical polishing, the surface of each sample is observed at various magnifications using a metallographic microscope, as shown in Fig. 1. The black regions in the figure represent the pores, while the gray regions represent the Ni-Zn ferrite coatings. Fig. 1 shows that both samples have well-formed Ni-Zn ferrite coating layers, with the 7.5 wt% sample exhibiting more complete ferrite layers and fewer pores compared to the 5 wt% sample.

**Table 1**
Relevant physical parameters of each sample.

| Sample | Ferrite content | Average density(g/cm$^3$) | Average resistivity (μΩ·m) |
|---|---|---|---|
| 1 | 5 wt% | 7.24 | 518 |
| 2 | 7.5 wt% | 6.99 | 730 |

Using the AMH-1M-S testing system (Fig. 2.), the magnetic properties of two types SMC ring samples are measured. The test excitations are quasi-static (10 Hz) and sinusoidal waves at 50 Hz and 100 Hz with different amplitudes. The primary winding has 100 turns, and the secondary winding has 15 turns.

## 3. Improved J-A hysteresis model

### 3.1. Static J-A model

The J-A model is predicated on the principle of magnetic domain wall movement, which delineates the actual magnetization $M$ into reversible magnetization $M_{rev}$ and irreversible magnetization $M_{irr}$ [21]:

$$M = M_{rev} + M_{irr} \tag{1}$$

Reversible magnetization occurs when the magnetization of a material changes in direct proportion to the applied magnetic field, and the material's magnetization can return to its original state once the external field is removed or reduced. And, irreversible magnetization refers to the magnetization that does not return to its original state when the external magnetic field is removed or reversed. This typically occurs due to the material undergoing changes like magnetic domain rearrangements, which are not fully recoverable.

The bending, movement, nucleation and annihilation of magnetic domain walls constitute the principal mechanisms underlying both the reversible and irreversible magnetization in Eq. (1), respectively. The ordinary differential equation describing irreversible magnetization is

$$\frac{\mathrm{d}M_{irr}}{\mathrm{d}H_{eff}} = \frac{\delta_M (M_{an} - M_{irr})}{k\delta} \tag{2}$$

where $M_{an}$ is the anhysteretic magnetization of ferromagnetic materials. And the anhysteretic magnetization refers to the magnetization of a material when the external magnetic field is gradually changed, without the influence of previous magnetic history or hysteresis. $\delta_M$ is a coefficient introduced to prevent the occurrence of a non-physical solution, $k$ is the pinning coefficient between magnetic domains, and $\delta$ is the directional coefficient. Given the similarity between ferromagnetic anhysteretic magnetization and paramagnetic alignment phenomena, the statistical ensemble-modified Langevin formalism is employed to model the Boltzmann distribution of the magnetic domain magnetization vectors [22]:

$$M_{an} = M_s[\coth\left(\frac{H_{eff}}{a}\right) - \left(\frac{a}{H_{eff}}\right)] \tag{3}$$

where $a$ is the effective magnetic domain density, $M_s$ is the saturation

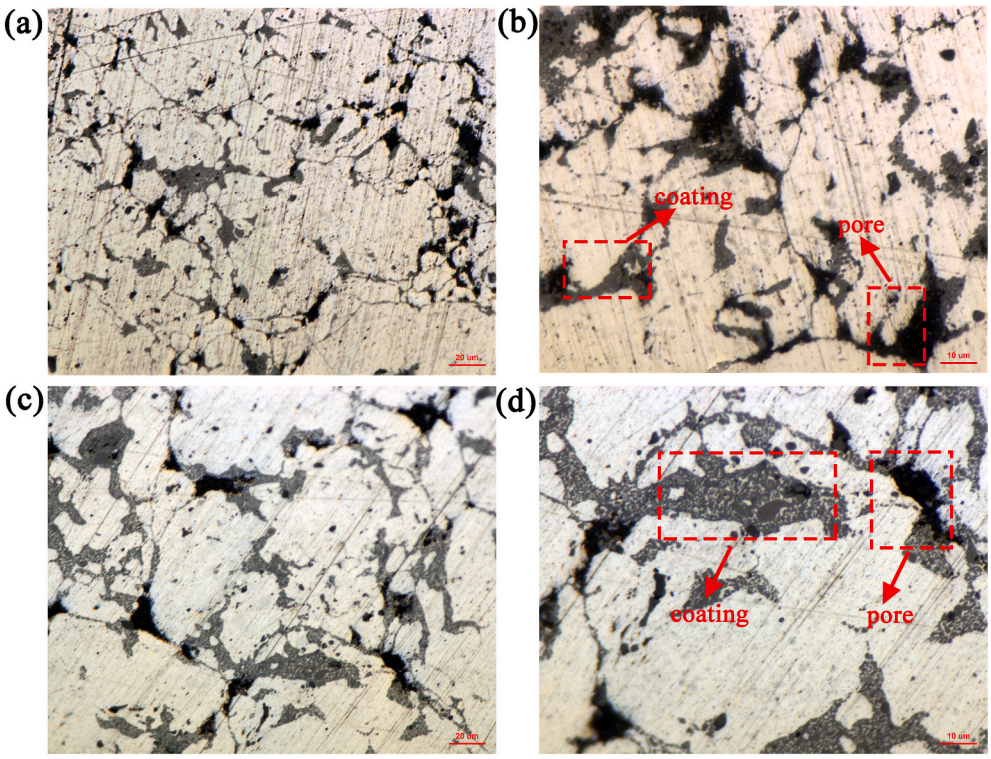



**Fig. 1.** Surface of 5 wt% Ni-Zn ferrite content sample at (a) 50 times magnification (b) 100 times magnification; 7.5 wt% Ni-Zn ferrite content sample at (c) 50 times magnification (d) 100 times magnification.




**Fig. 2.** Measuring equipment and samples.

magnetization, and $H_{eff}$ is the effective magnetic field intensity.

There is a relationship between the internal magnetic field $H_i$ and the effective magnetic field $H_{eff}$:

$$H_{eff} = H_i + \alpha M \tag{4}$$

$\alpha$ is the average coupling field parameter between magnetic domains. In laminated soft magnetic materials, when the material is magnetized along the in-plane direction, the demagnetization field inside the material becomes negligible, resulting in near-equivalence between the internal field $H_i$ and external field $H$. However, the microstructure of SMCs fabricated via powder metallurgy exhibits distinct characteristics – these materials comprise a multitude of ferromagnetic particles isolated by insulating coatings and interparticle pores. They can be considered as many isolated particles. During magnetization, each ferromagnetic particle develops an induced magnetic field influenced by its specific shape-dependent demagnetization factor [23]. This significantly impedes the external magnetization field, making it difficult for SMCs to reach saturation. For the quasi-ellipsoidal SMC particulates investigated in this study, according to Stratton's description of the behavior of ellipsoids with uniform permeability in a constant external field [24], the internal magnetic field $H_i$ and external magnetic field $H$ adhere to the following equation:

$$H_i = \frac{H}{1 + (\mu_r - 1)N_e} \tag{5}$$

$\mu_r$ is the relative permeability of the material, and $N_e$ is the effective demagnetization factor. Considering that magnetization $M$ also affects the demagnetization field, it is not comprehensive to describe the demagnetization effect between particles solely based on the shape demagnetization factor. Therefore, the comprehensive change in the demagnetization field is attributed to the effective demagnetization factor $N_e$. By substituting Eq. (5) into Eq. (4), the relationship between the effective field $H_{eff}$ and external field $H$ in the improved J-A model applicable to SMCs can be obtained as:

$$H_{eff} = \frac{1}{1 + (\mu_r - 1)N_e} H + \alpha M \tag{6}$$

According to the law of conservation of energy

$$\mu_0 \int M \mathrm{d}H_{eff} = \mu_0 \int M_{an} \mathrm{d}H_{eff} - \mu_0 k\delta(1-c) \int \frac{\mathrm{d}M_{irr}}{\mathrm{d}H_{eff}} \mathrm{d}H_{eff} \tag{7}$$

$\mu_0$ is the vacuum permeability, $c$ is the reversible magnetization coefficient. In practical applications, power devices typically function as voltage-type devices with specified voltages at both the terminals [17]. According to Faraday's law of electromagnetic induction, the input parameter in such devices is the magnetic induction intensity $B$, while

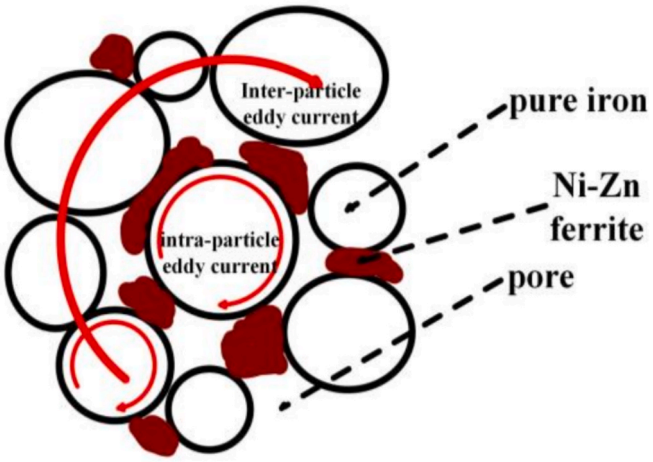



**Fig. 3.** Intra-particle and inter-particle eddy in SMCs.

the desired parameter is the magnetization $M$ or magnetic field intensity $H$. When $H_{eff}$ conforms to Eq. (4), the inverse model of the traditional J-A model is

$$\frac{dM}{dB}=\frac{\delta_m(M_{an}-M)+ck\delta\frac{dM_{an}}{dH_{eff}}}{\mu_0\left\{\delta k+(1-\alpha)\left[\delta_M(M_{an}-M)+ck\delta\frac{dM_{an}}{dH_{eff}}\right]\right\}} \tag{8}$$

When $H_{eff}$ conforms to Eq. (6), the J-A model is presented in the form of an inverse model:

$$\frac{dM}{dB}=\frac{\delta_m(M_{an}-M)+ck\delta\frac{dM_{an}}{dH_{eff}}}{\mu_0\left\{\delta k[1+(\mu_r-1)N_e]+\{1-\alpha[1+(\mu_r-1)N_e]\}\left[\delta_M(M_{an}-M)+ck\delta\frac{dM_{an}}{dH_{eff}}\right]\right\}} \tag{9}$$

### 3.2. Dynamic J-A model

As the operating frequency increases, iron losses in ferromagnetic materials include not only hysteresis losses but also frequency-dependent eddy current and excess losses. In 2011, Hamimid et al. proposed a modified dynamic J-A model based on the loss separation approach for a mixed magnetic field formula [25]. Due to the inter-particle insulation in SMCs, the traditional eddy current loss formula used for laminated materials like silicon steel is no longer applicable. In addition, SMCs sintered using SPS undergo a heating and cooling process which is similar to stress-relief annealing. This metallurgical treatment effectively diminishes residual lattice strains, resulting in domain configuration stabilization that suppresses excess loss contributions across the sub-20 kHz frequency spectrum.

According to the homogenization theory, the iron particles within SMCs can be modelled as ellipsoids of varying dimensions, as shown in Fig. 3. Due to the obstruction of air and high resistivity Ni-Zn ferrite, the eddy current losses ($P_e$) inside SMCs can be decomposed into inter-particle eddy current losses ($P_e^{inter}$) and intra-particle eddy current losses ($P_e^{intra}$) [7]:

$$P_e=P_e^{inter}+P_e^{intra}=(k_e^{inter}+k_e^{intra})B_m^2f^2 \tag{10}$$

$$k_e^{inter}=\frac{(\pi d)^2}{\beta\rho_{SMC}},\ k_e^{intra}=\frac{(\pi d_{Fe})^2}{6\rho_{Fe}} \tag{11}$$

**Table 2**
Relevant parameters of PSO algorithm.

| Parameter | Value |
|---|---|
| Number of cycles $z$ | 10 |
| Total number of iterations $K$ | 60 |
| Number of variables $d$ | 6 |
| Number of particles $n$ | 100 |
| Maximum personal learning factors $c_{1max}$ | 2 |
| Minimum personal learning factors $c_{1min}$ | 1.6 |
| Maximum social learning factors $c_{2max}$ | 1.9 |
| Minimum social learning factors $c_{2max}$ | 1.5 |
| Initial inertia weight $w_{start}$ | 0.9 |
| Final inertia weight $w_{end}$ | 0.5 |

$$\beta=\frac{6}{1-0.633\frac{w}{h}\tanh(\frac{1.58h}{w})} \tag{12}$$

Among them, $\rho_{SMC}$ and $\rho_{Fe}$ are the resistivity of SMCs and pure iron, $d$ is the shorter side of the cross-sectional rectangle of the ring sample, and $d_{Fe}$ is the average particle diameter of the iron particles. Given a substantial number of particles within the material, the particle size distribution approximates a Gaussian distribution, and the mean value of this distribution is utilized for the calculations. $\beta$ is the shape parameter of the sample cross-section, which is determined by the width ($w$) and height ($h$) of the sample cross-section. Substituting Eq. (10) into the energy balance equation to obtain the energy balance equation applicable to SMCs:

$$\oint_{cycle}H(B)\cdot dB=\oint_{cycle}H_{hyst}(B)\frac{dB}{dt}dt+\oint_{cycle}\frac{dW_e}{dt}dt \tag{13}$$

Among them: $\frac{dW_e}{dt}=(k_e^{inter}+k_e^{intra})(\frac{dB}{dt})^2$.

Because eddy current losses depend on the periodicity of the magnetic induction intensity $B$ and are independent of the changes in the magnetic field intensity $H$. The eddy current field $H_e$ can be decomposed into $H_e^{inter}$ and $H_e^{intra}$, and the expression for the effective magnetic field intensity $H_{eff}$ applicable to the dynamic J-A model can be obtained:

$$H_{eff}=\frac{\mu_0H}{\mu_0+(\mu_0\mu-\mu_0)N_e}+\alpha M-H_e \tag{14}$$

where $H_e=H_e^{inter}+H_e^{intra}=k_e^{inter}\frac{dB}{dt}+k_e^{intra}\frac{dB}{dt}$。

## 4. Model simulation and result analysis

### 4.1. The improved static J-A model simulation

Based on the measured hysteresis loops, the parameters of the traditional and improved J-A models in this study ($a$, $k$, $c$, $\alpha$, $M_s$, $N_e$) are identified using the particle swarm optimization (PSO) algorithm. The first step is to initialize a group of particles that are assigned random positions and velocities in the solution space of the problem. Then, in each iteration, the velocity of each particle is updated using the following equation:

$$v_i(t+1)=w\bullet v_i(t)+c_1\bullet r_1(pBest_i-x_i(t))+c_2\bullet r_2(gBest-x_i(t)) \tag{15}$$

$$c_1=c_{1max}-\frac{(c_{1max}-c_{1min})\bullet j}{K} \tag{16}$$

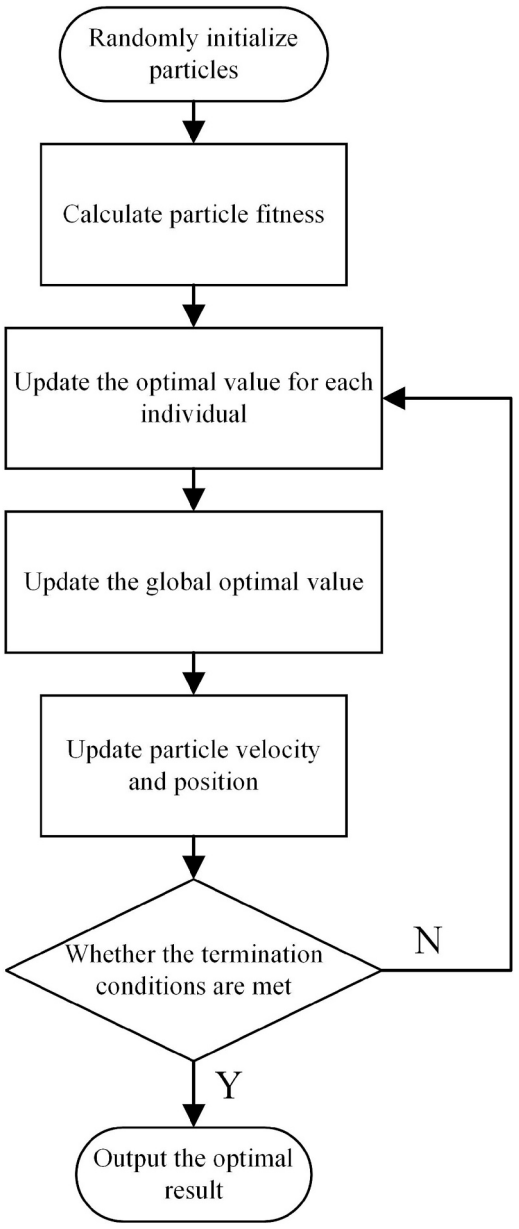



**Fig. 4.** The flowchart of PSO algorithm.

$$c_2 = c_{2min} + \frac{(c_{2max} - c_{2min}) \bullet j}{K} \tag{17}$$

$$w = w_{start} - \frac{(w_{start} - w_{end}) \bullet j}{K} \tag{18}$$

where, $v_i(t)$ is velocity of the i-th particle at time $t$. $w$ is inertia weight which controls how much the previous velocity influences the new velocity. $c_1$, $c_2$ are personal and social learning factors. $K$ is the total number of iterations. And during the execution of the algorithm, $w$, $c_1$, $c_2$ will dynamically change with the number of iterations $j$ to improve the iteration speed and convergence of the algorithm. $r_1$, $r_2$ are random values between 0 and 1. $pBest_i$ is the personal best position of the i-th particle. $gBest$ is the global best position of the swarm. $x_i(t)$ is position of the i-th particle at time $t$. After updating the velocity, each particle's position is updated accordingly. The relevant parameters of PSO are shown in Table 2, and the flowchart of PSO is shown in Fig. 4.

Table 3 lists the relevant parameters of the improved J-A model. Because the parameters of the J-A model have clear physical meanings, it is necessary to constrain the parameter values to comply with physical laws.

**Table 3**
Relevant parameters for the improved static J-A model.

| Ferrite content | $f$ (Hz) | $B$ (T) | $a$ (A/m) | $k$(A/m) | $c$ | $\alpha(10^{-4})$ | $M_s$(A/m) | $N_e$ |
|---|---|---|---|---|---|---|---|---|
| 5 wt% | 10 | 1.1 | 415 | 1587 | 0.62 | 5.9 | $1.38 \times 10^6$ | $2.26 \times 10^{-2}$ |
| | | 0.9 | 408 | 928 | 0.50 | 5.6 | $1.05 \times 10^6$ | $6.18 \times 10^{-3}$ |
| | 50 | 1.1 | 950 | 1518 | 0.43 | 10.0 | $1.49 \times 10^6$ | $1.26 \times 10^{-2}$ |
| | | 0.9 | 828 | 1480 | 0.16 | 9.5 | $1.32 \times 10^6$ | $2.67 \times 10^{-3}$ |
| 7.5 wt% | 10 | 1.0 | 357 | 2597 | 0.76 | 5.0 | $1.14 \times 10^6$ | $7.55 \times 10^{-2}$ |
| | | 0.8 | 272 | 1412 | 0.71 | 4.9 | $9.79 \times 10^5$ | $4.73 \times 10^{-2}$ |
| | 50 | 1.0 | 907 | 1353 | 0.71 | 13.9 | $1.09 \times 10^6$ | $3.86 \times 10^{-2}$ |
| | | 0.8 | 777 | 1266 | 0.54 | 10.0 | $9.44 \times 10^5$ | $1.25 \times 10^{-2}$ |

For each composite material, the improved J-A model parameters obtained are plotted in Fig. 5: (a), (d) effective magnetic domain density $a$;(b), (e) domain coupling parameter $\alpha$; (c), (f) effective demagnetization factor $N_e$. It is evident that for samples with high or low ferrite content, the effective magnetic domain density $a$ gradually increases with an increase in $B$. This is due to a stronger magnetic field leads to more intense magnetic domain wall activity and magnetic domain rotation, resulting in more effective magnetic domains. In addition, the parameter $\alpha$ that characterizes the strength of inter-domain coupling and the magnetic domain density $a$ show the same trend. A higher magnetic domain density leads to a denser magnetic domain structure, which enhances the inter-domain coupling strength. This collective magnetization behavior ultimately governs the observed enhancement of the inter-domain coupling strength.

According to E. Kneller's theory, the B-H curve can be segmented into low-field reversible loss regions and high-field irreversible loss regions [26]. The transition point between these two regions is the magnetic induction intensity $B_{\mu_{max}}$, which corresponds to the maximum effective permeability $\mu_{max}$. At this point, the dominant magnetization mechanism changes: Above $B_{\mu_{max}}$, irreversible magnetization prevails through Barkhausen-type domain wall displacement, while the region below $B_{\mu_{max}}$ demonstrates dominant reversible magnetization via coherent domain rotation mechanisms [27]. Experimental specimens with 5 wt% and 7.5 wt% ferrite concentrations exhibited characteristic $B_{\mu_{max}}$ values of 0.4 T and 0.2 T, respectively. The maximum magnetic flux density $B_{max}$ measured in this study is higher than $B_{\mu_{max}}$, therefore the materials exhibit both reversible and irreversible magnetization.

The influence of the demagnetization field is more pronounced in irreversible magnetization. Therefore, it is appropriate to incorporate the demagnetization coefficient into the improved model. Parametric analysis reveals that the demagnetization field, linearly dependent on magnetization $M$, progressively impedes both domain rotation and wall motion as $B$ increases. The effective magnetic field intensity $H_{eff}$ decreases at an accelerated rate under the influence of the demagnetization field. The increasing trend of the effective demagnetization factor $N_e$ with the increase in $B$, as shown in Fig. 5(c) and (f), provides empirical validation of this theoretical construct. At the same time, the

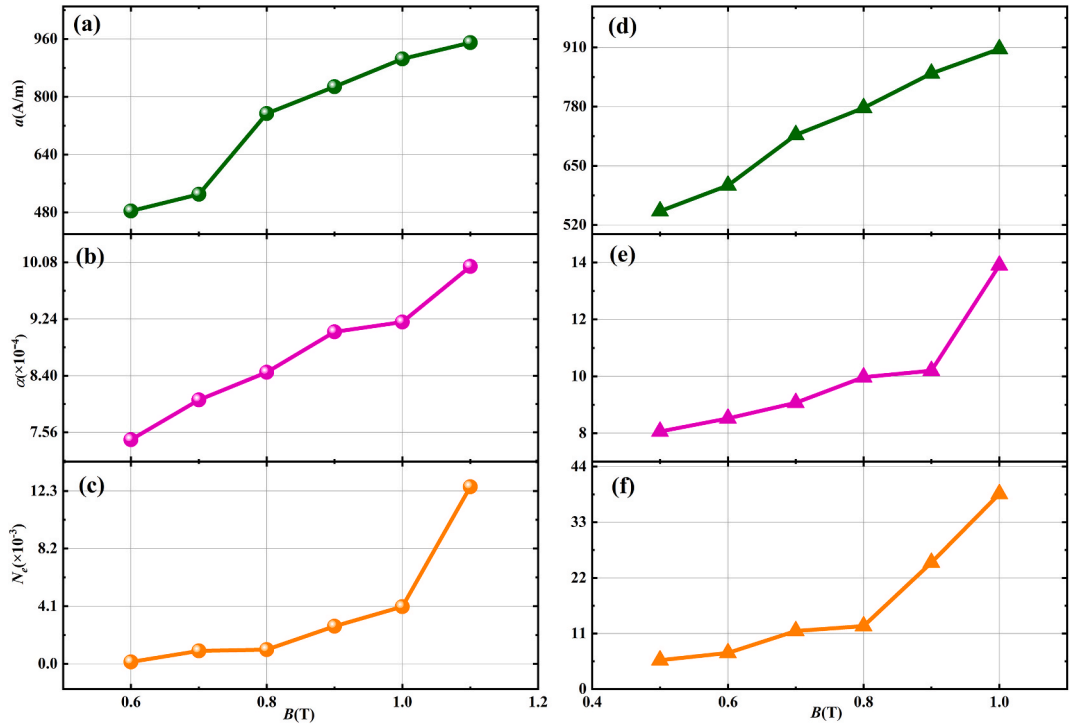



**Fig. 5.** Improved J-A model parameters: (a), (b), (c) 5 wt% ferrite content sample; (d), (e), (f) 7.5 wt% ferrite content sample.

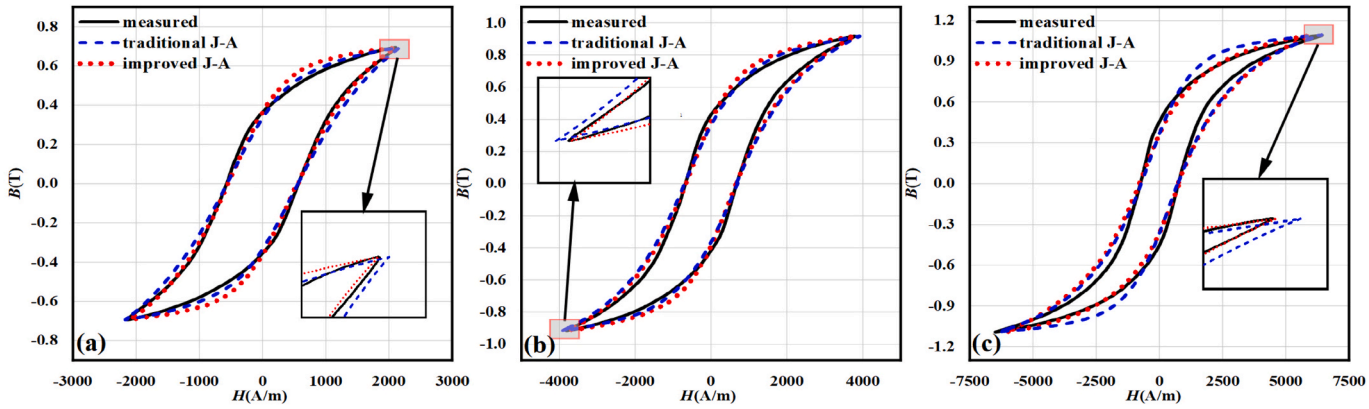



**Fig. 6.** B-H curves of 5 wt% ferrite content sample at 10 Hz (a) 0.7 T (b) 0.9 T (c) 1.1 T.

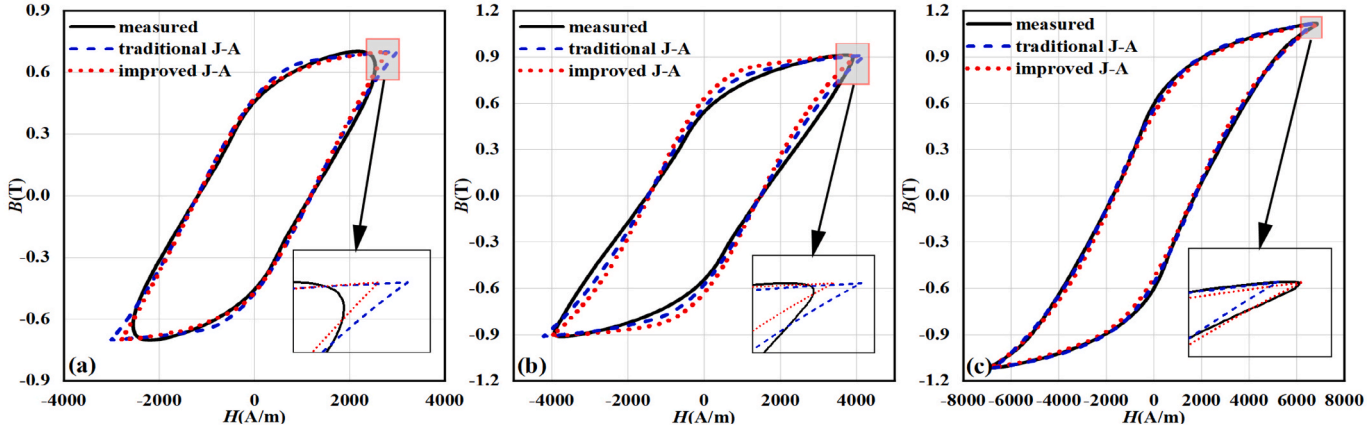



**Fig. 7.** B-H curves of 5 wt% ferrite content sample at 50 Hz (a) 0.7 (b) 0.9 T(c)1.1 T.

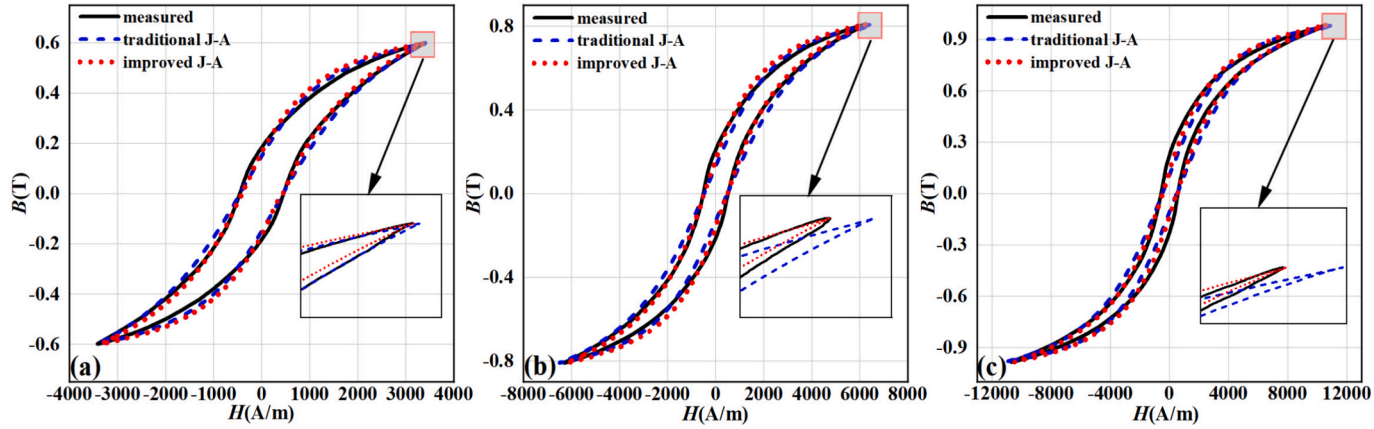



**Fig. 8.** B-H curves of 7.5 wt% ferrite content sample at 10 Hz (a) 0.6 T (b) 0.8 T(c)1T.

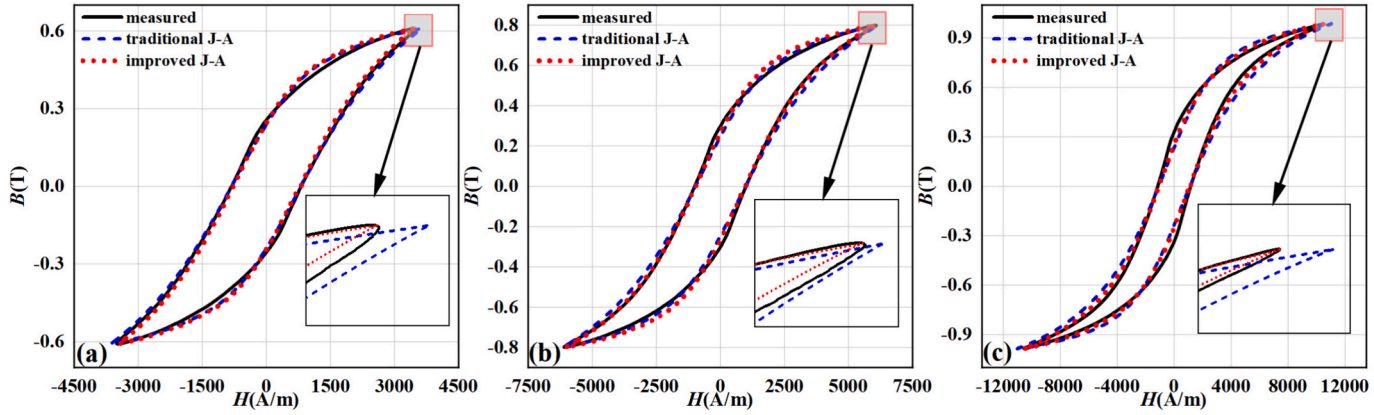



**Fig. 9.** B-H curves of 7.5 wt% ferrite content sample at 50 Hz (a) 0.6 T (b) 0.8 T(c)1T.

**Table 4**
Relevant parameters of static model loss errors for 5 wt% ferrite content samples.

| *f*(Hz) | *B*(T) | Error before improved | Error after improved |
|---|---|---|---|
| 10 | 0.7 | 10.99 % | 4.95 % |
| | 0.9 | 11.38 % | 3.96 % |
| | 1.1 | 6.78 % | 1.90 % |
| 50 | 0.7 | 3.20 % | 2.00 % |
| | 0.9 | 5.85 % | 1.23 % |
| | 1.1 | 5.07 % | 3.19 % |

**Table 5**
Relevant parameters of static model loss error for samples with 7.5 wt% ferrite content.

| *f*(Hz) | *B*(T) | Error before improved | Error after improved |
|---|---|---|---|
| 10 | 0.6 | 13.64 % | 7.37 % |
| | 0.8 | 10.70 % | 6.98 % |
| | 1.0 | 2.63 % | 1.56 % |
| 50 | 0.6 | 4.86 % | 3.03 % |
| | 0.8 | 6.54 % | 5.60 % |
| | 1.0 | 18.73 % | 0.69 % |

effective demagnetization factors $N_e$ of both materials decrease to a very small value when approaching $B_{\mu_{max}}$. Because diminished external field intensity near transition point reduces demagnetization field generation. At this time, the effective magnetic field $H_{eff}$ of the improved and traditional models are approximately equivalent, demonstrating model consistency across different magnetization regimes.

Considering that the general service conditions of iron-based SMCs is low frequency and high magnetic flux density, testing is carried out under these conditions. The hysteresis loops of the 5 wt% Ni-Zn ferrite sample at 10 Hz (Fig. 6), 50 Hz (Fig. 7), and the 7.5 wt% Ni-Zn ferrite sample at 10 Hz (Fig. 8) and 50 Hz (Fig. 9) are simulated. A comparison is conducted between the curves obtained by the traditional J-A model, the improved model and the measurement results.

For samples with 5 wt% ferrite content, the improved model enhances the simulation accuracy of the rising branch of the curve in the first quadrant compared to the traditional model at 10 Hz (Fig. 6), but there are notable differences between both the modelling and the measured curves. When the frequency increases to 50 Hz (Fig. 7), although both the traditional and improved models show high accuracy at 1.1 T, as the magnetic flux density decreases to 0.9 T, the curve exhibits no apparent saturation trend, and the accuracies of both models diminish rapidly. Nevertheless, the simulation locally enlarged images in Fig. 6 and Fig. 7 indicate that in the region near $B_{max}$ of the curve, the simulation accuracy of the improved model is substantially higher than that of the traditional model. The hysteresis modelling method is an effective way to calculate the iron losses of SMCs, so we use the relative error $\varepsilon_{loss}$ as the criterion of the accuracy of the hysteresis model:

$$\varepsilon_{loss} = \frac{|P_{model} - P_{measured}|}{P_{measured}} \times 100\% \tag{19}$$

where $P_{model}$ and $P_{measured}$ are the calculated iron losses of the J-A model and the measured iron losses. Table 4 lists the calculated and measured loss errors of the samples with 5 wt% ferrite content. The loss error of the improved J-A model is below 5 %, which is substantially lower than that

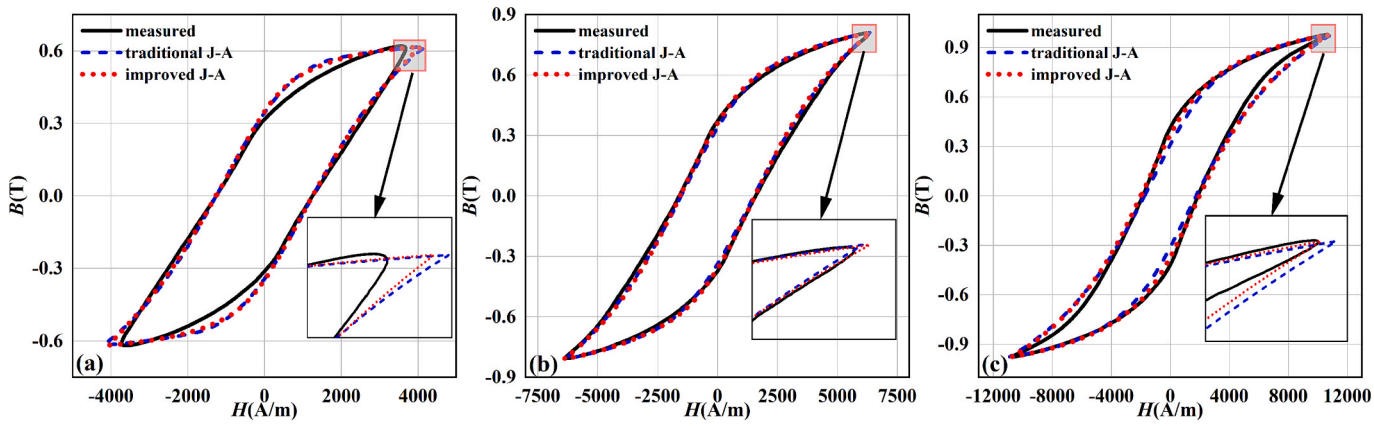



**Fig. 10.** B-H curve of 7.5 wt% ferrite content sample at 100 Hz (a) 0.6 T (b) 0.8 T (c) 1 T.

**Table 6**
Relevant parameters of the improved dynamic J-A model for SMC sample with 7.5wt% ferrite content.

| $B$(T) | $a$(A/m) | $k$(A/m) | $c$ | $\alpha(10^{-4})$ | $M_s$(A/m) | $N_e$ | $k_e^{inter}$ | $k_e^{intra}$ |
|---|---|---|---|---|---|---|---|---|
| 1.0 | 1288 | 3176 | 0.42 | 17.30 | $9.87 \times 10^5$ | $3.22 \times 10^{-3}$ | 0.0262 | 0.0442 |
| 0.8 | 1017 | 1937 | 0.21 | 6.42 | $9.19 \times 10^5$ | $3.71 \times 10^{-4}$ | | |
| 0.6 | 436 | 1336 | 0.14 | 0.97 | $6.12 \times 10^5$ | $2.27 \times 10^{-4}$ | | |

**Table 7**
Relevant parameters of model loss error for 7.5 wt% ferrite content sample at 100 Hz.

| $B$(T) | Error before improved | Error after improved |
|---|---|---|
| 0.6 | 8.07 % | 7.86 % |
| 0.8 | 4.26 % | 2.55 % |
| 1 | 5.04 % | 0.72 % |

of the traditional model. It is worth noting that, unlike the pattern at 10 Hz, the accuracy of the improved model at 50 Hz did not improve with the increase of magnetic flux density. Under the same magnetic flux density, as the frequency increases, the saturation trend of the SMCs gradually weakens, resulting in a decrease in the accuracy of the improved model.

The sample with 7.5 wt% ferrite content exhibits a lower saturation magnetic induction intensity and permeability compared to the sample with 5 wt% ferrite content, because it contains more soft magnetic ferrite with ferrimagnetism. For the sample with 7.5 wt% ferrite content, both the traditional and improved J-A models show improved simulation accuracy, with the improved model demonstrates superior precision near $B_{max}$. Moreover, as shown in Table 5, the error of the improved model remains substantially lower than that of the traditional model.

### 4.2. The improved dynamic J-A model simulation

The hysteresis loops of the sample with 7.5 wt% ferrite content at 100 Hz are simulated using the improved dynamic J-A model and compared with the measured loops, as shown in Fig. 10. The eddy current parameters $k_e^{inter}$ and $k_e^{intra}$ in the dynamic model can be calculated using Eq. (10), (11), and (12). The relevant parameters of the improved dynamic J-A model are listed in Table 6. Samples with a higher ferrite content exhibit superior soft magnetic properties at higher frequencies due to their increased electrical resistivity. When $B$ is higher than 0.6 T, the improved model has higher simulation accuracy in the rising and falling branches of the curve than the traditional model, which primarily affects the prediction of permeability. As the frequency increases, it becomes increasingly difficult for the material to reach saturation. Comparing Fig. 8 (a) and Fig. 10 (a), when the frequency increases from 10 Hz to 100 Hz, the hysteresis loop begins to approach a circular loop. At this point, the simulation accuracies of both the traditional and improved models begin to decline. However, the improved model still better simulates the curve details than the traditional model.

Table 7 presents the relevant parameters of the dynamic model loss error for samples with 7.5 wt% ferrite content at 100 Hz. At a high magnetic flux density, both the improved and traditional models have relatively small loss errors. As the magnetic flux density continues to decrease, the errors of both models increase, but the error of the improved model is always lower than that of the traditional model, with errors not exceeding 8 % at various magnetic flux densities. In the SMC sample with ferrite content of 7.5 wt%, there is no phenomenon that the accuracy of the improved model decreases with the increase of frequency and magnetic flux density. This is because with the increase of ferrite content in SMCs, the material has stronger anti-saturation ability and stronger adaptability to the model.

## 5. Conclusion

This paper investigates the effect of demagnetization field on the magnetization process of iron-based SMCs. Incorporate demagnetization correction into the effective field $H_{eff}$ to develop static and dynamic J-A models suitable for laboratory prepared iron-based SMCs with complex magnetic properties. To evaluate the effectiveness and accuracy of the model, iron-based SMCs with Ni-Zn ferrite contents of 5 wt% and 7.5 wt % are prepared. The excellent prediction accuracy of the improved J-A model has been validated through simulation and experiments. The average of the relative error of iron losses at low frequencies and near saturation magnetic flux density is 3.69 %. Especially at local area of the hysteresis curve, the improved model performs better.

Furthermore, the trends and underlying causes of the relevant parameters are analyzed from the perspective of the SMCs magnetization. The improved J-A model provides a more comprehensive explanation of the magnetization characteristics of SMCs. It is applicable to laboratory prepared SMCs and contributes to the optimization of material properties. However, for lower magnetic flux densities and B-H curves approaching minor circular loops, the model accuracy still requires improvement.

Based on precise modeling of iron-based SMCs at low frequencies and high magnetic densities, and with the help of microscopic magnetization theory, future research will focus on the magnetic properties of other SMCs at high frequencies (kHz) and low magnetic densities (lower than $B_{\mu_{max}}$).

## CRediT authorship contribution statement

**Zhang Changgeng:** Resources, Writing – review & editing, Supervision, Project administration, Funding acquisition. **Guo Ziran:** Methodology, Software, Validation, Formal analysis, Investigation, Data curation, Writing – original draft, Writing – review & editing. **Lin Zhiwei:** Conceptualization, Resources, Supervision, Project administration, Funding acquisition. **Li Yongjian:** Resources, Supervision, Project administration, Funding acquisition.

## Declaration of competing interest

The authors declare that they have no known competing financial interests or personal relationships that could have appeared to influence the work reported in this paper.

## Acknowledgments

This work was supported in part by the National Key R&D Program of China (No. 2023YFB3809200), the National Natural Science Foundation of China, (No. 52277008, 52130710), Natural Science Foundation of Hebei Province, China (No. E2023202050), and the Funds for Creative Research Groups of Hebei Province, China (No. E2024202298).

## Data availability

The data that has been used is confidential.

## References

[1] E.A. Périgo, B. Weidenfeller, P. Kollár, J. Füzer, Past, present, and future of soft magnetic composites, Appl. Phys. Rev. 5 (2018) 031301.
[2] T. Yang, K. Lu, J. Wang, J. Xu, Z. Zheng, X. Liu, Fe-6.5 wt%Si soft magnetic composites with significant improvement of magnetic properties by compositing nano-MnZn ferrites, J. Alloys Compd. 909 (2022) 164660.
[3] K.J. Sunday, M.L. Taheri, NiZnCu-ferrite coated iron powder for soft magnetic composite applications, J. Magn. Magn. Mater. 463 (2018) 1–6.
[4] W. Li, Particles size-dependent magnetic properties of a FeSiAl soft magnetic composite with hybrid insulating coating for MHz applications, Mater. Sci. 291 (2023) 116387.
[5] H. He, Y. Liu, Z. Cui, Z. Huang, Z. Wu, Q. Hou, High-performance Fe–6.5wt.%Si/CaCO3 soft magnetic composites prepared via the thermal decomposition of calcium acetate, J. Phys. Chem. Solids 190 (2024) 112012.
[6] C. Zhang, Z. Guo, Z. Lin, Y. Li, High performance soft magnetic composites based on Fe/Ni-Zn ferrite powder prepared by low-pressure spark plasma sintering, J. Alloys Compd. 1012 (2025) 178436.
[7] P. Kollár, Power loss separation in Fe-based composite materials, J. Magn. Magn. Mater. 327 (2013) 146–150.
[8] H. Shokrollahi, K. Janghorban, Soft magnetic composite materials (SMCs), J. Mater. Process. Technol. 189 (2007) 1–12.
[9] J.-L. Mattei, M.L. Floc'h, Percolative behaviour and demagnetizing effects in disordered heterostructures, J. Magn. Magn. Mater. 257 (2003) 335–345.
[10] G. Weir, W. Trompetter, J. Leveneur, N. Long, J. Turner, J. Kennedy, Theory of low loss minor loops in soft magnetic composites, J. Magn. Magn. Mater. 588 (2023) 171411.
[11] H. Zhang, Q. Yang, C. Zhang, Y. Li, Y. Chen, Magnetic properties simulation of electrical steel sheet based on recurrent neural network, IEEE Trans. Magn. 60 (2024) 1–4.
[12] R. Liu, C. Gu, J. Sun, F. Shu, B. Tang, Analytical inverse Preisach model and its comparison with inverse Jiles–Atherton Model in terms of accuracy and computational speed, IEEE Trans. Magn. 59 (2023) 1–5.
[13] H. Hauser, Energetic model of ferromagnetic hysteresis: Isotropic magnetization, J. Appl. Phys. 96 (2004) 2753–2767.
[14] D.C. Jiles, D.L. Atherton, Theory of ferromagnetic hysteresis (invited), J. Appl. Phys. 55 (1984) 2115–2120.
[15] D.C. Jiles, Frequency dependence of hysteresis curves in conducting magnetic materials, J. Appl. Phys. 76 (1994) 5849–5855.
[16] Z. Birčáková, P. Kollár, J. Füzer, R. Bureš, M. Fáberová, Magnetic properties of selected Fe-based soft magnetic composites interpreted in terms of Jiles-Atherton model parameters, J. Magn. Magn. Mater. 502 (2020) 166514.
[17] X. Zhao, D. Zhang, Z. Ren, K. Shi, Y. Zhang, An improved dynamic magnetic hysteresis model in soft magnetic composites, J. Magn. Magn. Mater. 597 (2024) 172021.
[18] Y. Li, Y. Li, Z. Lin, S. Yue, R. Chen, P. Guo, J. Liu, A hysteresis model for soft magnetic composites considering particle size distribution, IEEE Trans. Magn. 1–1 (2024).
[19] K. Shi, D. Zhang, Z. Ren, D. Chen, Y. Zhang, C.-S. Koh, Effect of particles size on Eddy-current loss of soft magnetic composites using combined DEM and FEM, IEEE Trans. Magn. 60 (2024) 1–8.
[20] X. Yu, Y. Li, Q. Yang, S. Yue, C. Zhang, Loss characteristics and model verification of soft magnetic composites under non-sinusoidal excitation, IEEE Trans. Magn. 55 (2019) 1–4.
[21] K. Chwastek, Modelling of dynamic hysteresis loops using the Jiles–Atherton approach, Math. Comput. Model. Dyn. Syst. 15 (2009) 95–105.
[22] R. Szewczyk, Validation of the anhysteretic magnetization model for soft magnetic materials with perpendicular anisotropy, Materials 7 (2014) 5109–5116.
[23] G. Weir, Approximate shape factors for soft magnetic composites, J. Magn. Magn. Mater. 541 (2022) 168557.
[24] J.A. Stratton, Electromagnetic Theory, McGraw-Hill, New York, 1941.
[25] M. Hamimid, Hybrid magnetic field formulation based on the losses separation method for modified dynamic inverse Jiles–Atherton model, Phys. B 406 (14) (2011) 2755–2757.
[26] E. Kneller, A. Seeger, H. Kronmüller, Ferromagnetismus, Springer, Berlin Heidelberg, Berlin, Heidelberg, 1962, pp. 30–37.
[27] Z. Birčáková, F. Onderko, S. Dobák, P. Kollár, J. Füzer, R. Bureš, M. Fáberová, B. Weidenfeller, J. Bednarčík, M. Jakubčin, J. Szabó, M. Dilyová, Eco-friendly soft magnetic composites of iron coated by sintered ferrite via mechanofusion, J. Magn. Magn. Mater. 543 (2022) 168627.